# Convective mass transfer around a dissolving bubble

Jerome Duplat
*Univ. Grenoble Alpes, CEA, INAC-SBT, F-38000 Grenoble, France*

Mathieu Grandemange
*Michelin Research Center, ZI Ladoux, 63118 Cebazat, France*

Cedric Poulain*
*Univ. Grenoble Alpes, CEA, LETI MINATEC Campus, F-38000 Grenoble, France*
(Received 4 January 2017; published 22 November 2017)

Heat or mass transfer around an evaporating drop or condensing vapor bubble is a complex issue due to the interplay between the substrate properties, diffusion- and convection-driven mass transfer, and Marangoni effects, to mention but a few. In order to disentangle these mechanisms, we focus here mainly on the convective mass transfer contribution in an isothermal mass transfer problem. For this, we study the case of a millimetric carbon dioxide bubble which is suspended under a substrate and dissolved into pure liquid water. The high solubility of $CO_2$ in water makes the liquid denser and promotes a buoyant-driven flow at a high (solutal) Rayleigh number ($\mathrm{Ra} \sim 10^4$). The alteration of $p$H allows the concentration field in the liquid to be imaged by laser fluorescence enabling us to measure both the global mass flux (bubble volume, contact angle) and *local* mass flux around the bubble along time. After a short period of mass diffusion, where the boundary layer thickens like the square root of time, convection starts and the $CO_2$ is carried by a plume falling at constant velocity. The boundary layer thickness then reaches a plateau which depends on the bubble cross section. Meanwhile the plume velocity scales like $(dV/dt)^{1/2}$ with $V$ being the volume of the bubble. As for the rate of volume loss, we recover a constant mass flux in the diffusion-driven regime followed by a decrease in the volume $V$ like $V^{2/3}$ after convection has started. We present a model which agrees well with the bubble dynamics and discuss our results in the context of droplet evaporation, as well as high Rayleigh convection.

DOI: 10.1103/PhysRevFluids.2.114001

## I. INTRODUCTION

In the last 30 years, much work has been devoted to the apparently simple problem of understanding how a sessile liquid droplet evaporates on a substrate; see Ref. [1] for a review. After the pioneering work of Deegan [2] and the "coffee-stain" effect, most work has been focused on the assumed diffusion-driven evaporation and its associated local divergence of the evaporation rate at the triple line (up to microscopic scales). This assumption leads to a global mass flux proportional to the drop perimeter, $\rho dV/dt \propto R$, or equivalently to $dV/dt \propto V^{1/3}$ with $V$ the drop volume and $R$ the drop radius. A large amount of literature has been devoted to this issue since experiments carried out in different conditions of temperature, substrate nature and wettability, or liquid nature often revealed some deviations with the expected temporal evolution or scaling law of the mass flux [3].

Classically, most experiments rely on image acquisition of the droplet (from above or aside) along time, leading (after some assumptions on the droplet shape: spherical cap or flat puddle) to the temporal evolution of the wetted radius $R$, droplet volume $V$, and contact angle $\Gamma_c$, giving

*cedric.poulain@cea.fr

 

the *total* mass flux $\dot{m}(t)$. In our opinion, further progress has been slowed down overall by the lack of techniques enabling a *local* mass flux measurement in the vapor phase around the drop, or equivalently, in the liquid phase around a bubble. In particular, most models rely on the assumption of a diffusion-driven evaporation yielding to the above mentioned divergence of the evaporation rate at the triple line, but no definitive experimental evidence of this has been given to date.

As outlined quite recently in this long history [4–6] the thermal Rayleigh number associated with the problem is such that the convection cannot, in general, be discarded even for a drop of water at room temperature and could be the dominant mechanism in some circumstances. Unfortunately, very few papers address the problem of controlling or measuring the humidity, which is a key parameter because it drives the mass flux. Additionally, visualization of the vapor field around an evaporating liquid drop is quite challenging, and so far only a handful of groups have been able to visualize and quantify the concentration field [7,8] in the case of liquid drops.

The complexity of evaporation near a triple line is noticeably due to the interplay between diffusive and convective evaporation, contact line pinning, and hydrodynamic flow due to Marangoni flows if temperature or concentration gradients develop during the process. Therefore, it is interesting to define simple situations where only a limited number of these effects come into play. For example, the process of gas dissolution or solubilization is in general much more isothermal than that of evaporation, and no singularity of the heat flux is expected. No significant temperature gradient can develop, hence Marangoni flows will play no role; however, the question of the local repartition of the flux still remains. Correlatively, it would be instructive to have a highly convective mass transfer instead of an intermediate diffuso-convective regime in which both mechanisms are competing.

These conditions can be fulfilled with a bubble of a highly soluble gas dissolving in water: the bubble vanishes, the triple line advances, and mass transfer can be diffusion- or convection-driven. In such a dissolution process, the bubble vanishes because of the concentration (or equivalently partial pressure) unbalance between the bubble content of $CO_2$ (at saturation at the interface) and the $CO_2$ concentration away from the interface (outside the boundary layer). In that sense and like the droplet evaporation issue, both mass diffusion and convection are driven by the difference of concentration between the interface and the bulk far from the spherical interface, which are more or less far from saturation depending on whether the droplet is heated or not.

Similarly and after a phase of diffusion, a locally higher concentration creates an overweight of the fluid rising (or falling) away from the drop or the bubble. Like in the thermal case it is possible to define a *solutal* Rayleigh number [5]. In the present paper it is defined in terms of the solute boundary layer thickness $\delta_{CO_2}$:

$$\mathrm{Ra} = \frac{g\frac{\Delta\rho}{\rho}\delta_{CO_2}^3}{\nu D}, \tag{1}$$

with $\nu$ and $D$, respectively, the kinematic viscosity and the $CO_2$ diffusion coefficient in water, $\Delta\rho/\rho$ the relative excess density, and $\delta_{CO_2}$ the typical length scale of density gradients. In the same way as its thermal analogous, this Rayleigh number is a measure of the destabilizing effect, namely, density gradients (here induced by concentration of a dissolved compound) competing with two stabilizing mechanisms, which are viscosity and mass (instead of heat diffusion).

The questions that follow are these: What is the concentration distribution and its associated scaling? Is this law very different from that obtained in a diffusion-driven regime when Ra is small? Thus, the aim of the present paper is to examine the role played by natural convection solely, in the absence of heat flux, and to identify which scaling law is obtained when convection alone is present.

Here we present experiments enabling local $CO_2$ concentration field measurements around a $CO_2$ bubble dissolving in water at ambient pressure and temperature suspended from a teflon substrate. The "sessile bubble" is formed on the lower surface of a flat teflon substrate and condenses in a vessel containing water and fluorescein (see Fig. 1).

The choice of the $CO_2$ has been made for several reasons. First, $CO_2$ is one of the most soluble gases in water, it dissolves quickly, and the increase of $CO_2$ concentration in the surrounding water

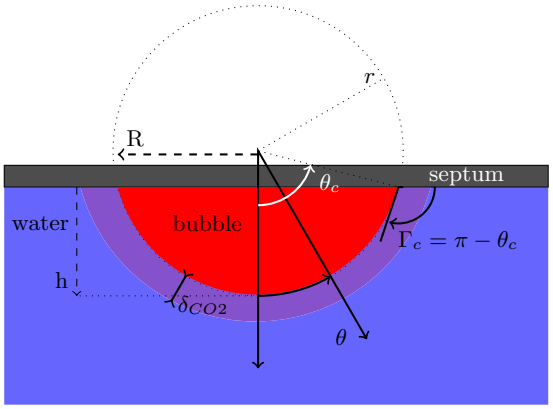


FIG. 1. Sketch of the $CO_2$ sessile bubble (in red) along with the notations used in the paper. $R$ is the radius of the dry area, $\Gamma_c$ the contact angle, and $\theta$ the current angle on the bubble. $\theta = 0$ is the apex of the bubble. The $CO_2$ boundary layer (in the liquid phase) is drawn in dark blue around the bubble interface.

promotes buoyancy effects and can trigger natural convection-driven mass transfer. Second, unlike other common gases ($N_2$, $H_2$, $O_2$, etc), dissolved $CO_2$ chemically reacts with water and produces protons, altering the $p$H. Thus, assuming chemical equilibrium, it is possible to determine a local dissolved $CO_2$ concentration in the water given a local $p$H measurement. Finally, in the context of climate change, a new technique for studying $CO_2$ dissolution in a diffusive or convective regime) is still worth of interest, either for $CO_2$ sequestration [9] or more generally for improving the $CO_2$ impact estimations [10].

Indeed, by using both a fluorescent pH sensitive compound and an adequate laser planar sheet to excite the fluorescence it is possible to map a two-dimensional (2D) concentration field anywhere in a transparent aqueous medium. This technique, called Planar Laser Induced Fluorescence (PLIF), has been widely and successfully used in order to probe scalar fields in recent decades [11–14]. Here the PLIF technique has been implemented and calibrated to achieve the quantitative $p$H and hence $CO_2$ concentration field measurement. The fluorescein has been chosen because its fluorescence depends on its chemical environment ($p$H) [15]. Thus, PLIF gives us access to the instantaneous concentration field around the dissolving bubble, and by adding the instantaneous bubble geometry (volume) one can obtain local and global mass transfer properties.

## II. EXPERIMENTAL SECTION

$CO_2$ dissolution in pure water is a well-known multistep reaction [16]. Considering liquid water in contact (at the liquid interface) with a gaseous carbon dioxide atmosphere of partial pressure $P_{CO_2}$, the reaction proceeds according to

$$\begin{aligned} CO_2(g) &\rightleftharpoons CO_{2(aq)}, \quad H = 30.1\ \text{atm}\,\text{l}\,\text{mol}^{-1}\ [17], \\ CO_{2(aq)} + H_2O &\rightleftharpoons H^+ + HCO_3^-, \quad pKa_1 = 6.35, \\ HCO_3^- &\rightleftharpoons H^+ + CO_3^{2-}, \quad pKa2 = 10.33, \\ H_2O &\rightleftharpoons H^+ + HO^-, \quad pKa_w = 14, \end{aligned}$$

where $Ka_1 = 10^{-pKa_1} = \frac{[HCO_3^-][H^+]}{[CO_{2(aq)}]}$, $Ka_2 = 10^{-pKa_2} = \frac{[CO_3^{2-}][H^+]}{[HCO_3^-]}$, and $K_w = 10^{-pK_w} = [H^+][HO^-]$ are the equilibrium constants of the chemical reactions, and $H = P_{CO_2}/[CO_{2(aq)}]$ is the Henry constant. For the sake of simplicity, we have neglected the hydrated form of dissolved carbon dioxide ($CO_{2(aq)} + H_2O \rightleftharpoons H_2CO_3$) because of its very slow kinetic compared to the other reactions.

We define the concentration relation $C_T = [CO_{2(aq)}] + [HCO_3^-] + [CO_3^{2-}]$ and the proton condition of pure solution $[H^+] = [HCO_3^-] + 2[CO_3^{2-}] + [HO^-]$, which both must be verified at all times. This system of equations leads to a global equilibrium between the different species yielding only one $p\mathrm{H} = -\log[H^+]$ for an imposed $CO_2$ partial pressure given by

$$P_{CO_2} = H \times \frac{10^{-p\mathrm{H}} - 10^{p\mathrm{H}-p\mathrm{K}_w}}{2 \times 10^{2p\mathrm{H}-p\mathrm{Ka}_1-p\mathrm{Ka}_2} + 10^{p\mathrm{H}-p\mathrm{Ka}_1}}. \tag{2}$$

Typically, pure water in equilibrium with a 1 atm partial pressure of $CO_2$ is at $p\mathrm{H} \approx 4$. The kinetics of $CO_2$ dissolution is extremely rapid (the reaction rate is of order $10^{10}$ $s^{-1}$), while the protons production rate is 3 $s^{-1}$ [18]). These chemical time scales are significantly smaller than hydrodynamics ones ($t^* \sim 20$ s) as will be discussed further. For sake of simplicity, in the following, we will consider chemical reaction as instantaneous.

In our case, we want to probe the $p\mathrm{H}$ field so that a $p\mathrm{H}$-sensitive compound (namely fluorescein) has to be added [11]. Consequently, a chemical reaction between the fluorescent dye and the aqueous solution takes place, shifting the equilibrium. The fluorescent dye is dissolved at a concentration of 2 mg/l in ultrapure water. However, as we have calculated, it is possible to show that the amount of fluorescent dye introduced is quite negligible with respect to the amount of dissolved $CO_2$. Thus, one may consider the relation (2) valid.

Fluorescein used in this paper is disodium fluorescein ($C_{20}H_{10}Na_2O_5$, $M = 376.28$ g/mol) hereafter abbreviated as Fl. It is a tribase salt soluble in aqueous solutions. It decomposes into four subspecies: $H_3Fl^+$, $H_2Fl$, $HFl^-$, and $Fl^{2-}$ [15]. It is possible to show that the respective amount of each species is a function of $p\mathrm{H}$ and namely that in our range of interest ($4 < p\mathrm{H} < 7$), the dominant species responsible for fluorescence is $Fl^{2-}$ [19]. The fluorescence is such that the absorption spectrum is peaked around 490 nm, and the fluorescence (reemission) spectrum is peaked at a wavelength of 515 nm (Stokes shift). For a given light source of unit intensity, a portion $F$ of this light is reemitted and is proportional to the amount of $Fl^{2-}$ in solution, which is itself a function of $p\mathrm{H}$. To get quantitative measurements of the $p\mathrm{H}$ field, a calibration procedure was developed and is detailed in the dedicated Supplemental Material [27].

The aim of our experimental setup is to create, at $t = 0$, a $CO_2$ bubble, in the most gentle and accurate manner, deposited on the underside of a substrate. The bubble will dissolve along time, and the associated $CO_2$ concentration field will be imaged by the PLIF technique. The $CO_2$ bubble is injected into a waterproof and transparent quartz vessel (see Fig. 2) filled with about 0.2 l of a water-fluorescein mixture. The bubble is created at the bottom side of a substrate which is a circular teflon septum of diameter 30 mm and thickness 2 mm. Instead of using a capillary tube to gently deposit the bubble on the surface of the substrate that caused undesired movements and concentration gradients in the surrounding liquid we have injected the bubble trough the septum itself: a needle (0.4 mm in diameter, 16 mm in length) is mounted on a micrometer stepper motor (Newport, model NSC200) over the upper side of the septum allowing accurate vertical translation along the $y$ axis. This system enables us to pierce the septum, create the desired bubble, and take the needle off without any $CO_2$ source remaining in the liquid. Each septum is used only once although it is waterproof for a few experiments. The $CO_2$ supply (air liquid, purity of 99.95%) at the needle inlet is controlled via a manometer at $P_{CO_2} = 1$ bar. The distance of the bubble to the bottom of the tank is kept constant and equal to 4 cm. To probe a 2D field of the $p\mathrm{H}$ concentration around the sessile dissolving bubble, a vertical laser sheet is implemented to match a bubble diameter and to be orthogonal to the camera focal plane, outside the tank. The laser is a Melles Griot ($\lambda = 488$ nm) of adjustable power ($\mathcal{P}_{\max} = 300$ mW) operating at a constant power of 280 mW during an experiment. The laser beam is directed using two mirrors directed at the bubble position. In order to transform the Gaussian circular laser beam into a planar sheet, two converging lenses are combined and adjusted to get the thinner and the most homogeneous sheet in the tank. The sheet thickness was estimated to be roughly 50 $\mu$m using the micrometric displacement of the tank. The video imaging system is a sensitive black-and-white 12-bit camera (PCO SENSICAM, model 630047) enabling frame resolution of

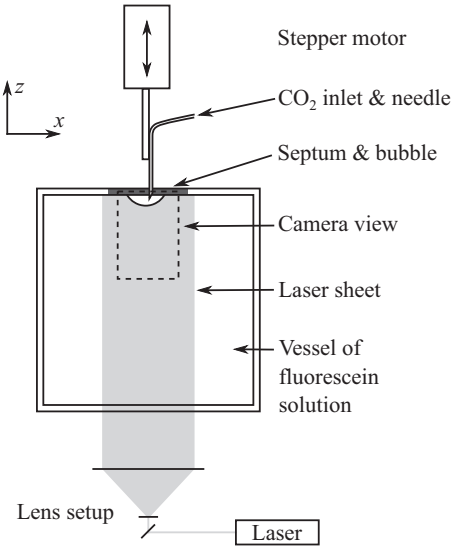


FIG. 2. Simplified sketch of the setup: the bubble is injected on the lower face of a teflon septum by piercing it with a very thin needle. The laser sheet enters the quartz vessel and illuminates a diametral plan of the bubble. The vessel is a 6 cm transparent cube made of quartz glass.

$1024 \times 1280$ mixels mounted with a Nikkon macrolens (50 or 105 mm depending on experiments) Emission spectra being peaked around $\lambda = 515$ nm, an interferometric filter is mounted on the camera to eliminate the excitation wavelength. Fluorescein being sensitive to temperature, short laser exposures are necessary to avoid photobleaching or thermoconvection effects. For that reason, a fast shutter (Newport, model 845HP) is placed on the laser path to stop illumination between two consecutive frames. This shutter is synchronized to the camera, which is itself connected together with the stepper motor to a PC. The whole setup is mounted on a Newport anti-vibration table.

## III. RESULTS AND DISCUSSION

As soon as the $CO_2$ is supplied and the needle pierces the septum substrate, a bubble is formed under the roof of the experimental cell (Fig. 3). During a typical dissolution, the sequence is the following: The fluorescence of fluorescein in the bubble neighborhood is drastically reduced, and a dark region appears around the bubble. Indeed, when the $CO_2$ dissolves in water, the water acidity increases (weaker fluorescence for acidic regions). This boundary layer thickens until it becomes unstable: a "heavy" plume then develops before sinking towards the bottom of the tank. During the whole process (typically 500 s), the bubble keeps dissolving into the water but never vanishes due to nonperfect purity of the injected bubble (typically, about 5% of the initial volume remains because of the presence of noncondensable gases).

A direct consequence of $CO_2$ dissolution is the bubble volume reduction. Like the problem of drop evaporation, this process proceeds in successive stages for the triple line dynamic. Classic backlight illumination as well as image processing of the dissolving bubble's contour confirm a systematic behavior for the triple line movement:

(1) At $t = 0$ (bubble formation), the contact angle is $\Gamma_c \approx 90^\circ$.

(2) For a typical duration of 120 s (depending on the initial volume of the bubble) the triple line remains pinned until the contact angle $\Gamma_c$ reaches the *advancing* angle $\Gamma_c \sim 110$–$140^\circ$. In this short phase, the base radius $R$ is roughly constant.

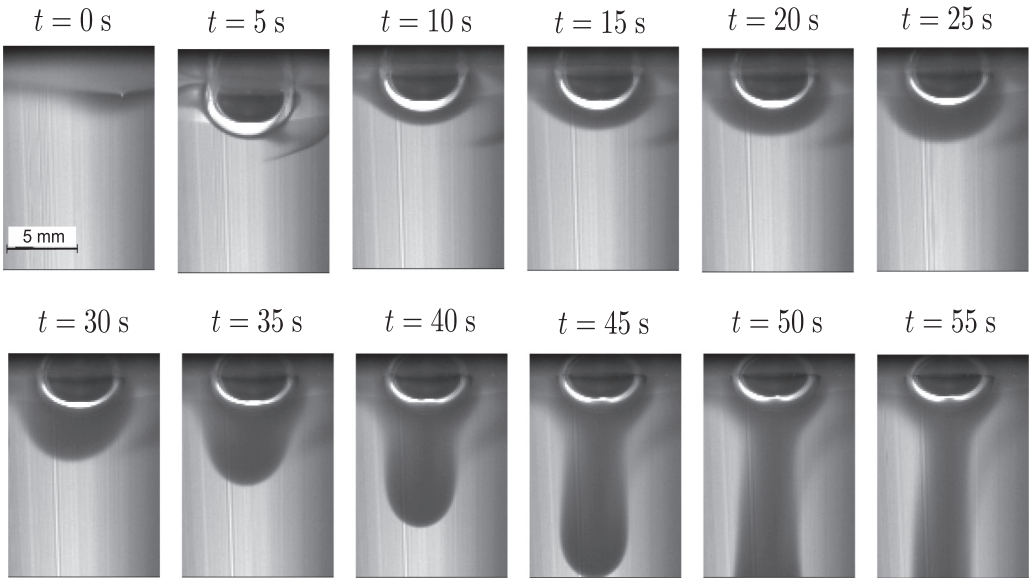


FIG. 3. Typical $CO_2$ bubble dissolution created with a partial pressure of 1 bar in a water + fluorescein ($[Fl^*] = 2$ mg/l) solution initially at $pH = 6.5$. The bubble's initial volume is $V = 37$ mm$^3$. A video and its associated concentration field are available at Ref. [27].

(3) Once unpinned, the triple line advances with a roughly constant contact angle close to the advancing one. This phase lasts until equilibrium is reached which occurs for a nonempty bubble because of the gas purity.

A typical video sequence for a carbon dioxide bubble of initial volume $V_0 = 25$ mm$^3$ is presented in the Supplemental Material [27] along with the associated processed video. Each image is processed in order to extract quantitative measurements of the angular profile of the $CO_2$ boundary layer thickness $\delta_{CO_2}$ as well as the bubble volume $V$, radius $R$, and contact angle $\Gamma_c$.

The development of the solute boundary layer around the bubble exhibits two consecutive stages: Immediately after creation, the boundary layer is thinner at the triple line and increases toward the apex. In that period, it thickens homogeneously all around the bubble so that the boundary layer thickness $\delta_{CO_2}$ increases with time according to

$$\delta_{CO_2} \propto \sqrt{t} \tag{3}$$

and is (hardly) independent on the position all around the bubble interface given by the angle $\theta$ (taking $\theta = 0$ at the bubble apex). All along this diffusion-driven process, no convection is observed anywhere in the tank.

From time $t^* \approx 20$ s after the bubble creation, the boundary layer gets unstable and a solute plume is formed at the bubble apex. It induces a global flow around the bubble from its base towards its apex. Simultaneously, the temporal evolution of the boundary layer is drastically modified: for a fixed angular position $\theta$, the thickness increases very rapidly and eventually reaches a plateau after just a few seconds (Fig. 4). The amplitude of this plateau depends on $\theta$. For a given time, the thickness is a decreasing function of $\theta$, i.e., $\delta_{CO_2}$ increases when moving from the base to the apex where it nearly diverges close to the apex where the plume develops.

It is observed (Fig. 5) that

$$\delta_{CO_2}(\theta)\sin(\theta) \approx \text{const.} \tag{4}$$

The boundary layers flows from the bubble base towards the apex. The local perimeter of the drop thus decreases as $2\pi r \sin(\theta)$. The boundary layer thickens when it flows along the bubble, and the

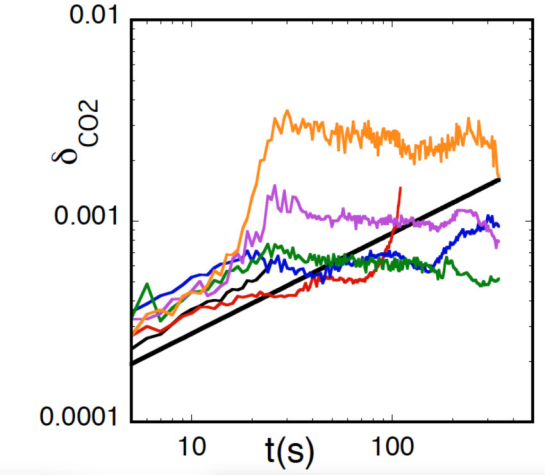


FIG. 4. Temporal evolution of the $CO_2$ boundary layer thickness $\delta_{CO_2}$ at various angles $\theta$ around the bubble (100°, 80°, 60°, 40°, 20°, and 0° (vertical direction) resp. black, red, blue, green, purple, and orange curves). The straight line corresponds to Eq. (8).

observed behavior indicates that the boundary layer cross section $2\pi r \sin(\theta)\delta(\theta)$ is constant along the bubble

The plume tip has a typical mushroom shape, clearly visible due to the strong inhibition of the fluorescence, so that the plume tip location can be easily determined. After a short period of acceleration (starting from zero velocity at detachment), the plume descent quickly reaches a plateau (constant velocity) hereafter referred as the "stationary" regime on which we are going to concentrate.

Figure 6 illustrates the stationary plume velocity as a function of the rate of volume loss, obtained for different initial bubbles of different volumes. One can observe that the plume velocity $v_p$ increases like $(dV/dt)^{1/2}$. The bubble volume variation $dV/dt$ is proportional to the mass of $CO_2$ dissolved in water and is carried by the falling solute plume.

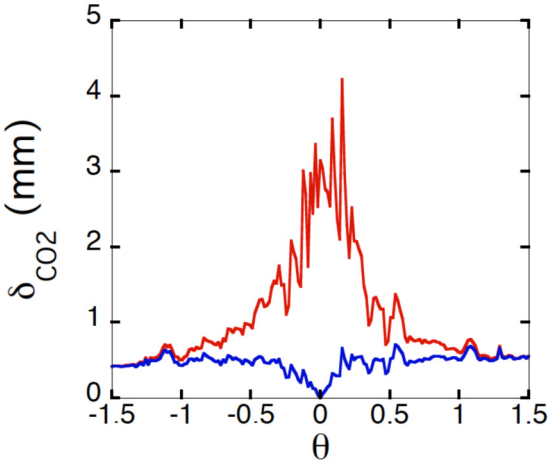


FIG. 5. Angular profile of the boundary layer thickness $\delta_{CO_2}$ (red) and of $\delta_{CO_2}\sin(\Gamma_c)$ (blue). Both are plotted along the coordinate $\theta$ (radian) for $t > t^*$. The corrected thickness is nearly constant: $\delta_{CO_2}\sin(\theta) \approx 0.5$ mm.

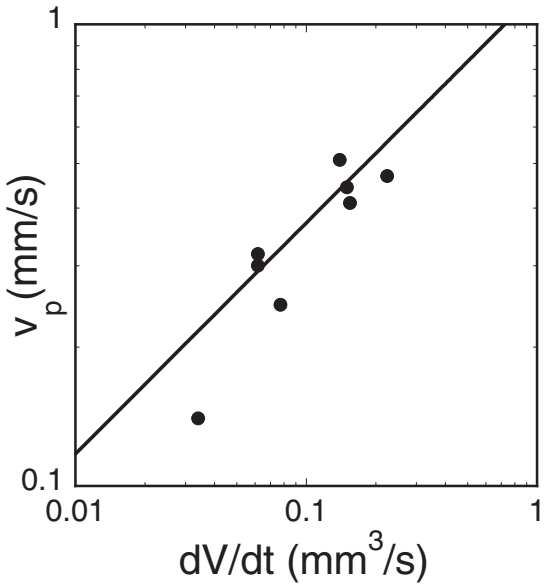


FIG. 6. Plume velocity $v_p$ for several experiments as a function of the averaged rate of volume loss. The reference line corresponds to Eq. (11).

As mentioned earlier, the initial content of the bubble is not pure $CO_2$. Its initial proportion $x_{CO_2}(0)$ is given by

$$x_{CO_2}(0) = \frac{V(0) - V_\infty}{V(0)}. \tag{5}$$

The evolution law of $V(t)$ differs in the first (diffusive) and second (convective) stage (See Fig. 7). In the first stage, before the plume develops and while the contact line is pinned, the volume $V(t)$ decreases linearly with respect to time. In the second stage, $V(t)$ nearly fits an exponential decrease. As the partial pressure of $CO_2$ decreases with time (it is close to 1 at the initial time, and becomes null

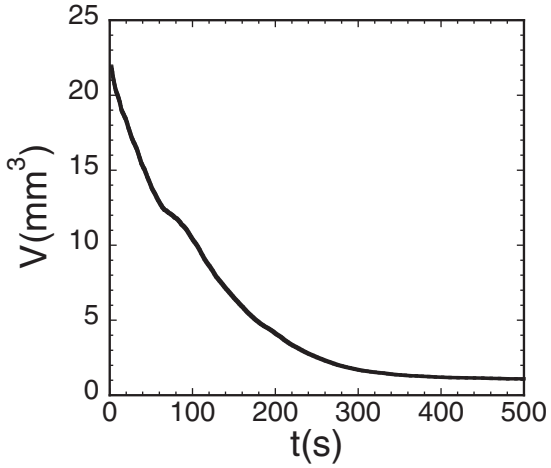


FIG. 7. Volume of a dissolving $CO_2$ bubble as a function of time.

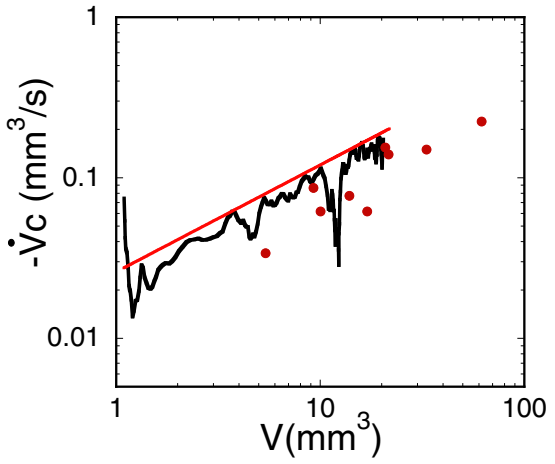


FIG. 8. Corrected condensation rate $\dot{V}_c$ as a function of volume: temporal evolution for a typical experiment (black curve), condensation rates for a collection of experiments (red points). The red line is the theoretical prediction from Eq. (14), which predicts a dependency as $V^{2/3}$ (where the only adjustable parameter is set to $\alpha = 2$).

at the end), the vanishing rate $-dV/dt$ is artificially reduced: the condensation flux is proportional to the molar fraction of $CO_2$ inside the bubble. This is particularly critical in the final instants. In order to correct this artifact, the corrected vanishing rate

$$-\dot{V}_c = -\frac{1}{\mathrm{x}_{\mathrm{CO}_2(t)}}\frac{dV}{dt} \tag{6}$$

is plotted as a function of $V(t)$. It is observed (Fig. 8) that, after the triple unpins

$$-\dot{V}_c \propto V^{2/3}. \tag{7}$$

This dependence seems contradictory to the apparent exponential decrease. However, the evolution law (7) predicts that the volume vanishes in a finite time $t_v$ like $V(t) \propto (t_v - t)^3$, which can be clearly distinguished from an exponential decrease only when $V(t)$ vanishes.

At the initial instant, the $CO_2$ bubble is created in a $CO_2$-free water environment. At the interface, the chemical disequilibrium is compensated for: the $CO_2$ vapor gets dissolved and expands diffusively according to

$$\delta_{\mathrm{CO}_2} = 2\sqrt{D_{\mathrm{CO}_2} t}, \tag{8}$$

with $D = 1.9 \times 10^{-9}$ m$^2$/s the aqueous $CO_2$ diffusion coefficient. Density of water $\rho$ in this boundary layer is increased by the dissolved $CO_2$:

$$\Delta\rho = M_{\mathrm{CO}_2} P_{\mathrm{CO}_2}/H,$$

with $M_{\mathrm{CO}_2} = 44$ g/mol the molar mass of $CO_2$.

This configuration is unstable, and a concentration plume is quickly formed and plunges downwards, as soon as the solutal Rayleigh number exceeds a critical value $\mathrm{Ra}_c$. We thus can anticipate a starting time for the plume given by

$$t^* = \left(\frac{\mathrm{Ra}_c \nu}{8\frac{\Delta\rho}{\rho} g D^{1/2}}\right)^{2/3}. \tag{9}$$

To the best of our knowledge, no value for a critical Rayleigh number around a hemispherical object has been reported in the literature. In the thermal case, however, Ref. [20] indicates that for thermal

plumes starting from rigid cylindrical (but not spherical) heater, the critical Rayleigh is $\mathrm{Ra}_c = 1100$. Assuming this value still holds with a bubble geometry and a moving interface, we anticipate a starting time for the plume $t^* \approx 0.33\mathrm{Ra}_c^{2/3} \approx 33$ s in good agreement with the observed starting time ($t^* \approx 20$ s).

The concentrated plume sinks towards the bottom of the tank. The excess weight of the plume is an immediate consequence of the dissolution of $CO_2$ in the boundary layers. The quantity of matter transported by the plume is then related to the bubble volume variation $dV/dt$. The typical radius of the plume is of the order of 1 mm, when the typical velocity is of the order of 1 mm/s. The Reynolds number associated with the plume is then of order 1, indicating a laminar flow. The velocity of the plumes is given by a balance between buoyancy forces and viscous drag. Previous studies [21–23] indicate that (again for thermal plumes) in a fluid of density $\rho$ and dynamic viscosity $\mu = \rho\nu$:

$$v_p = \left[\frac{\log(\epsilon^{-2})}{2\pi}\right]^{1/2}\left(\frac{\dot{m}g}{\mu}\right)^{1/2}, \tag{10}$$

where $\epsilon$ is the solution of $\epsilon^4 \log(\epsilon^{-2}) = \nu/D$ leading to a prefactor $[\log(\epsilon^{-2})/2\pi]^{1/2} \approx 0.77$, and $\dot{m}$ represents the total mass reduction rate in the vicinity of the heater. In our case, the mass flux is given by the bubble condensation rate $\dot{m} = \rho_{\mathrm{gas}}\dot{V}$.

In our experiments, we observe (Fig. 6) a prefactor of 0.28 instead of 0.77 for the thermal case. This scaling seems correct, although the different prefactor probably stems from the geometry of our problem, which is closer to a hemispherical sphere on a plan than to a cylinder in a free space:

$$v_p = 0.28\left(\frac{\rho_{\mathrm{gas}}\dot{V}g}{\mu}\right)^{1/2}. \tag{11}$$

The plume induces a flow around the bubble which deforms and stretches the concentration boundary layers. This flow field is tangential to the bubble walls except near the apex of the bubble. The velocity at the bubble wall is maximal and scales like the plume velocity $v_p$. Streamlines skirt the spherical bubble. They converge toward the apex of the bubble, in such a way that they are contorted. The typical stretching rate of this flow is given by the ratio of the typical length $R$ and typical velocity $V_p$. Assuming mass conservation between the streamlines converging towards the apex, and a constant velocity, the concentration boundary layer thickness is estimated by

$$\delta_0 = \delta_{\mathrm{CO_2}}(\theta)\sin(\theta) = \alpha\sqrt{\frac{DR}{\mathrm{v_p}}}, \tag{12}$$

where $\alpha = 2$ is an *ad hoc* numeric parameter.

The dissolution flux can now be estimated:

$$\Phi = \int_{\Gamma_c}^{0} 2\pi R^2 \sin(\theta)\frac{D[\mathrm{CO_2}]_{\mathrm{eq}}}{\delta_{\mathrm{CO_2}}}\,d\theta. \tag{13}$$

As $\dot{V} = V_M\Phi$, one finally obtains the equation for the volume variation:

$$\dot{V} = 0.42\mathrm{V}^{2/3}\left[\frac{\Delta\rho G(\Gamma_c)}{\alpha\rho_{\mathrm{gas}}}\right]^{4/3}\left(\frac{D^2\rho_{\mathrm{gas}}g}{\mu}\right)^{1/3}, \tag{14}$$

where

$$G(\Gamma_c) = \frac{2\pi[\Gamma_c/2 - \sin(2\Gamma_c)/4]}{\{4/3\pi[2+\cos(\Gamma_c)]\sin(\Gamma_c/2)^4\}^{1/2}} \tag{15}$$

is a geometric prefactor [$G(\pi/2) = 3.4$]. Equation (14) is plotted next to the experimental results in Fig. 8.

Using Eq. (11) together with the definition of $\delta_0$, the result

$$\delta_0 = \alpha^{4/3}\left(\frac{D\nu}{0.42\{\frac{\Delta\rho}{\rho}g[\Gamma_c/2 - \sin(2\Gamma_c)/4]\}}\right)^{1/3} \tag{16}$$

is established. A numerical application gives $\delta_0 = \alpha^{4/3}\, 7.5457 \times 10^{-5} = 2$ mm.

## IV. SUMMARY AND CONCLUSION

In this paper, we have studied the dissolution of a carbon dioxide bubble by means of a laser induced fluorescence technique. The bubble first dissolves in water by diffusion, and at time $t^*$ a convective plume starts to form at the bubble apex and carries the vapor away from the vanishing bubble. The laminar model presented here agrees with the observed tendencies. In particular, we were able to predict the time $t^*$ of the onset of convection when the boundary layer reaches a thickness such that a critical Rayleigh number (based on this thickness) has a critical value $\mathrm{Ra}_c \approx 1100$. It is noteworthy that this criterion implies that convection is inefficient at early stages. Thus, it could never be fulfilled for tiny bubbles which would dissolve before the boundary layer becomes unstable.

Assuming a low Reynolds plume, we predict a fall velocity which scales like the square root of the mass flux [Eq. (11)] in good agreement with the fall velocity measurements. Likewise, and taking the nonperfect purity of the gas into account, we obtain a prediction for the rate of volume loss [Eq. (14). This law is in reasonable agreement with both instantaneous and averaged experiments on different initial bubble volumes (Fig. 8).

Transposition of these scaling laws to the problem of evaporation deserves a special discussion. If we come back to the thermal problem of droplet evaporation, we can estimate the onset of convection for a drop of water in a dry atmosphere: at room temperature, the water vapor partial pressure is 25 mbar in the drop vicinity, while it is 0 beyond the boundary layer. Given the respective molar mass of air and vapor (ratio of about 2), $\Delta\rho/\rho \approx -0.1\%$ is a good approximation in these conditions. Hence, the critical Rayleigh $\mathrm{Ra}_c = 1100$ is reached when the light vapor boundary layer $\delta_{H_2O}$ reaches 1 cm, which is obtained at $t^* \approx 10$ s. Given that a millimetric water droplet takes a few hundred seconds to evaporate, convection can start quite early in the process. The scaling of Eq. (14) shows that our bubbles have a mass flux proportional to the bubble's surface while evaporating drops are closer to the diffusive regime with a flux proportional to the drop perimeter. Actually, the macroscopic Rayleigh number Ra based on the drop or bubble radius $\mathrm{Ra} = g(\Delta\rho/\rho)R^3/(D\nu)$ (with $D$ and $\nu$ respectively the diffusion coefficient and viscosity of the vapor) is about $\mathrm{Ra} = 1$ for a millimetric drop of water in a dry air, and $\mathrm{Ra} = 10^4$ for the millimetric bubbles of $CO_2$ studied in the present paper. In a nondimensional form, Eq. (14) is written $\mathrm{Sh} \sim \mathrm{Ra}^{1/3}$ with Sh the Sherwood number expressing the ratio of convective to diffusive flux. Interestingly, this law is coherent with the $\mathrm{Sh} \sim \mathrm{Ra}^{1/4}$ recently observed [8] for alcohol drops dissolving in water at intermediate Rayleigh numbers ($\mathrm{Ra} < 10^4$). Indeed, a transition of the scaling exponent from 1/4 to 1/3 for increasing Rayleigh numbers is also well established in the thermal case [24] where Sh has to be replaced by the Nusselt number Nu. Although convection is present and starts early in both evaporation and condensation problems, the Rayleigh number close to unity along with the scaling exponent confirms that the mass transfer is mainly diffusion-driven in the drop evaporation.

Equivalently, and assuming a constant contact angle process [so that $R(t) \sim h(t)$], we have $V \sim R^2 h \sim R^3$. After integration, Eq, (14) yields $R(t) \sim (t_v - t)$ where $t_v$ is the vanishing time. In other words, our results, obtained in an ultimate regime at high Rayleigh numbers, show that when convection is dominant, we have $R \sim (t_v - t)^n$ with $n = 1$ This scaling exponent is of course different from the scaling exponent of $n = 0.5$ obtained for a purely diffusive process. It is known [4,25] that scaling exponents increase for the most light and volatile vapors, and that $n$ varies from 0.5 for alkanes, to 0.57 for cyclohexane to as high as 0.68 for water. Our work thus confirms that $n$ is an indicator of the importance of convection with an upper limit of $n = 1$ at high Rayleigh numbers and gives a model for this regime.

To conclude, we also would like to emphasize the appeal of this approach for other fields of fluid mechanics, in addition to the climate change issue mentioned in the introduction. Use of $CO_2$ in conjunction with fluorescent imaging enables us to not only to visualize mass transfer in a flow but also to achieve very high Rayleigh conditions. For Rayleigh-Benard convection, high Rayleigh conditions are in general very difficult to reach at the laboratory scale and often require cryogenic conditions [26], and new approaches are probably welcome. In the Supplemental Material [27], we give an example of a Ra $\approx 10^7$ flow reached in a 1 cm square vessel, which we hope will stimulate future work in this field.

## ACKNOWLEDGMENT

The authors thank C. Kevorkian for his technical support, Dr. C. Vanhaverbeke for her help in chemistry, and S. Phaneuf for her careful reading of the manuscript.

[1] H. Yildirim Erbil, Evaporation of pure liquid sessile and spherical suspended drops: A review, Adv. Colloid Interface Sci. **170**, 67 (2012).
[2] R. D. Deegan, O. Bakajin, and T. F. Dupont, Capillary flow as the cause of ring stains from dried liquid drops, Nature (London) **389**, 827 (1997).
[3] C. Poulard, G. Guéna, A.-M. Cazabat, A. Boudaoud, and M. Ben Amar, Rescaling the dynamics of evaporating drops, Langmuir **21**, 8226 (2005).
[4] N. Shahidzadeh-Bonn, S. Rafaï, A. Azouni, and D. Bonn, Evaporating droplets, J. Fluid Mech. **549**, 307 (2006).
[5] O. Carrier, N. Shahidzadeh-Bonn, R. Zargar, M. Aytouna, M. Habibi, J. Eggers, and D. Bonn, Evaporation of water: Evaporation rate and collective effects, J. Fluid Mech. **798**, 774786 (2016).
[6] F. Carle, B. Sobac, and D. Brutin, Experimental evidence of the atmospheric convective transport contribution to sessile droplet evaporation, Appl. Phys. Lett. **102**, 061603 (2013).
[7] S. Dehaeck, A. Rednikov, and P. Colinet, Vapor-based interferometric measurement of local evaporation rate and interfacial temperature of evaporating droplets, Langmuir **30**, 2002 (2014).
[8] E. Dietrich, S. Wildeman, C. W. Visser, K. Hofhuis, E. S. Kooij, H. J. W. Zandvliet, and D. Lohse, Role of natural convection in the dissolution of sessile droplets, J. Fluid Mech. **794**, 45 (2016).
[9] J. A. Neufeld, M. A. Hesse, A. Riaz, M. A. Hallworth, H. A. Tchelepi, and H. E. Huppert, Convective dissolution of carbon dioxide in saline aquifers, Geophys. Res. Lett. **37**, L22404 (2010).
[10] S. Solomon, Gian-Kasper Plattner, R. Knutti, and P. Friedlingstein, Irreversible climate change due to carbon dioxide emissions, Proc. Natl. Acad. Sci. U. S. A. **106**, 1704 (2009).
[11] I. Houcine, H. Vivier, E. Plasari, R. David, and J. Villermaux, Planar laser induced fluorescence technique for measurements of concentration fields in continuous stirred tank reactor, Exp. Fluids **22**, 95 (1996).
[12] W. Asher and J. F. Pankow, Direct observation of concentration fluctuations close to a gas-liquid interface, Chem. Eng. Sci. **44**, 1451 (1989).
[13] T. Munsterer and B. Jahne, Lif measurements of concentration profiles in the aqueous mass boundary layer, Exp. Fluids **25**, 190 (1998).
[14] G. Herlina and H. Jirka, Application of lif to investigate gas transfer near the air-water interface in a grid-stirred tank, Exp. Fluids **37**, 341 (2004).
[15] M. Martin and L. Lindqvist, The ph dependance of fluorescein fluorescence, J. Lumin. **10**, 391 (1975).
[16] W. Stumm and J. J. Morgan, *Aquatic Chemistry*, 3rd ed. (John Wiley & Sons, New York, 1996).
[17] I. Dalmolin, E. Skovroinski, A. Biasi, M. L. Corazza, C. Dariva, and J. V. Oliveira, Solubility of carbon dioxide in binary and ternary mixtures with ethanol and water, Fluid Phase Equilib. **245**, 193 (2006).
[18] M. J. Mitchell, O. E. Jensen, K. A. Cliffe, and M. M. Maroto-Valer, A model of carbon dioxide dissolution and mineral carbonation kinetics, Proc. R. Soc. Lond. A **466**, 1265 (2010).

[19] H. Diehl and R. Markuszewski, Studies on fluorescein—VII: The fluorescence of fluorescein as a function of pH, Talanta **36**, 416 (1989).
[20] C. M. Vest and M. L. Lawson, Onset of convection near a suddenly heated horizontal wire, Int. J. Heat Mass Transfer **15**, 1281 (1972).
[21] G. K. Batchelor, Heat convection and buoyancy effects in fluids, Q. J. R. Meteorol. Soc. **80**, 339 (1954).
[22] E. Moses, G. Zocchi, and A. Libchaberii, An experimental study of laminar plume, J. Fluid Mech. **251**, 581 (1993).
[23] E. Kaminski and C. Jaupart, Laminar starting plumes in high-Prandtl-number fluids, J. Fluid Mech. **478**, 287 (2003).
[24] A. Bejan, *Convection Heat Transfer* (John Wiley & Sons, New York, 2013).
[25] M. Cachile, O. Benichou, C. Poulard, and A. M. Cazabat, Evaporating droplets, Langmuir **18**, 8070 (2002).
[26] J. J. Niemela, L. Skrbek, K. R. Sreenivasan, and R. J. Donnelly, Turbulent convection at very high Rayleigh numbers, Nature (London) **404**, 837 (2000).
[27] See Supplemental Material at http://link.aps.org/supplemental/10.1103/PhysRevFluids.2.114001 for a raw and its associated processed videos of the dissolution of a bubble and a video of a high Rayleigh convection in a tank together with additionnal informations about the calibration procedure.